Measuring fluid structural interaction on a cantilevered panel using optical fiber Bragg gratings

Luke Pollock[1], Harald Kleine[2], Andrew Neely[3], and Graham Wild.[4]
University of New South Wales, Canberra, ACT, 2612, Australia

This work explores the use of optical fiber Bragg gratings (FBGs) to measure the Fluid Structural Interaction (FSI) on a cantilever panel. While ground testing makes use of an array of experimental techniques to measure vibrations from FSI, many cannot be incorporated in flight-test or production vehicles where measurements of FSI are needed, particularly at hypersonic speeds. The use of FBGs leverages previous work on Structural Health Monitoring (SHM) where the sensing technology can be applied to detect an array of different measurands, including dynamic strain. Initial work presented includes simulation of sensor response using different interrogation techniques. A two-dimensional, steady-state, one-way coupling approach is used to determine the deformation and strain of several cantilever panels at Mach 2 and Mach 3 conditions. The dynamic response of the cantilever was then used to predict the response of the FBG sensor. These results will be compared to upcoming validation experiments that will utilize the supersonic blowdown wind tunnel at UNSW Canberra.

Nomenclature

DOFSS	=	distributed optical fiber sensing systems
FBG	=	fiber Bragg gratings
FSI	=	fluid-structure interactions
FTSI	=	fluid-thermal-structure interactions
SHM	=	structural health monitoring
OFS	=	optical fiber sensors
EMI	=	electromagnetic interference
C2	=	command & control
TDM	=	time division multiplexing
WDM	=	wavelength division multiplexing
COTS	=	commercial off the shelf
CFD	=	computational fluid dynamics
SST	=	shear stress transport
RANS	=	Reynolds averaged Navier-Stokes
SNR	=	signal-to-noise ratio
LP-FBG	=	long period fiber Bragg grating
FWHM	=	full width half maximum

[1] Research Associate, School of Engineering & Information Technology, AIAA Member
[2] Associate Professor, School of Engineering & Information Technology.
[3] Associate Dean of Research Engagement, Professor, School of Engineering & Information Technology, AIAA Associate Fellow.
[4] Senior Lecturer, School of Engineering & Information Technology, AIAA Member.

I. Introduction

While mechanical failures are a significant concern in commercial air transport [1], the harsh nature of hypersonic flight and the toll it has on structures is evident by the relatively high failure rates during operation of hypersonic vehicles [2]. There are many case studies that exemplify this, for example DARPA's Falcon HTV-2 which most likely suffered an "unexpected aeroshell degradation" [3]. Such failures result because supersonic and hypersonic vehicles are subject to Fluid-Thermal-Structural Interactions (FTSI) at high speeds. This is due to their mass-constrained design and the severe aerothermodynamic loads. These interactions can adversely affect the ability of the vehicle to fulfil its mission due to the reduction in stiffness and strength of the structure, which results in thermoelastic and thermoplastic structural distortion and reduced life [4], as well as reduced aerodynamic and propulsive performance. Whilst there is a need to ensure hypersonic vehicles utilize high quality materials free of defects [5], monitoring of FTSI inflight is essential to assess inflight shape distortion [6]. The concept of a "failure detection system" for hypersonic vehicles was discussed by Kirkham and Hunt in 1977 [7]. As such, there is a growing effort to quantify the effects of FTSI as well as develop and validate the necessary numerical tools to confidently design mass-efficient yet robust vehicles [8]. However, these efforts have been held back by a lack of high-fidelity experimental data for code development and validation. A majority of the previous (limited) experimental efforts in the literature have conducted tests in very short duration (typically less than 1 sec) hypersonic wind tunnels, where the models remain essentially isothermal, but this has allowed researchers to decouple the thermal aspects of the problem to focus on the underlying high-speed Fluid-Structural Interactions (FSI) while still allowing some thermal effects to be simulated by appropriate selection of material stiffnesses on the experimental models [9-11].

The monitoring of structural distortion in flight requires very different sensing and instrumentation systems to those typically utilized in ground-based testing. Parameters of interest can vary spatially and temporarily facilitating the need for advanced sensing systems. Distributed Optical Fiber Sensing Systems (DOFSS) possess the required properties. In fact, while some conventional sensing technologies will also be applicable, the immunity to electromagnetic interference, the light weight, the ability to operate at elevated temperatures, and the versatility make optical Fiber Bragg Gratings (FBGs) ideally suited to the task. There is a direct analog for the application of this research in future launch vehicles for data acquisition, towards greater understanding of the flow physics as well as quasi-real-time Command and Control (C2) functionality. The high multiplexing capabilities of FBG sensors present the possibility of order of magnitude increases in sensor quantities and hence, the production of data, in comparison to historical hypersonic programs [12, 13]. Hypersonic flight test programs have demonstrated a disproportionate number of sensors dedicated for the measurement of FTSI with most sensors employed to study the near field aerodynamics. Whilst strain gauges and thermocouples can measure FTSI phenomena each sensor provides a discrete, single point measurement. Hence, the requirements for full field structural monitoring results in large increases in complexity and weight. Moreover, the limited capabilities of these sensors restrict the amount of data that can be generated from experiments in ground test facilities. The development of a distributed sensing system that can remain lightweight and sensitive dramatically improves the amount of data that can be collected and hence accelerates the ability to understand FTSI phenomena both fundamentally and in-flight. A distributed sensing system is likewise required for the realization of design concepts employing morphing geometries where structural shape sensing must be monitored in real-time, often in extremely harsh environments [14].

As an alternative to traditional strain gauges and thermocouples, Optical Fiber Sensors (OFS) present as a superior alternative for the measurement of FTSI for both flight and ground tests with numerous advantages, including [15]:

- excellent sensitivity,
- small size,
- low weight,
- immunity to Electromagnetic Interference (EMI) (and hence, plasma effects),
- low cost,
- extremely versatile,
- extremely reliable, and
- compatible with optical communications (including fly-by-light systems [16]).

The EMI immunity of OFS and fiber optic systems as well as the ability to operate fly-by-light [16], is a significant advantage for hypersonic vehicle structures. That is, potential immunity from interference from plasma sheaths generated during high energy flight [17].

Whilst a variety of OFS technologies exist, including interferometric, scatter, and FBGs, FBGs are easy to multiplex and are extremely versatile. FBGs have been used to sense and monitor static strain, temperature, pressure, radiation, corrosion, and dynamic strain, such as vibration, ultrasound, acousto-ultrasonics, and acoustic emissions [18]. Specifically, as temperature sensors, FBGs have been reported in applications up to 1500 K in silica fiber and 2000 K in sapphire fiber [19]. As such, FBGs are ideally suited for the development of an integrated distributed sensing network for the measurement of FTSI.

FBGs are spectrally reflective elements in the core of an optical fiber. The grating is created by forming a series of periodic variations in the refractive index of an optical fiber core, resulting in the formation of a Bragg reflector that functions as a wavelength specific mirror [20]. The change in the reflected wavelength, also known as the Bragg wavelength, can be determined as a function of the local strain and temperature. Hence, by tracking the change in the Bragg wavelength, the strain and temperature at the grating can be determined. The change in the Bragg wavelength is related to the mechanical strain and temperature through equation (1). The constants k_ϵ and k_T represent the sensitivity of the FBG to each measurand.

$$\frac{\Delta\lambda_B}{\lambda_B} = k_\epsilon \epsilon + k_T \Delta T \quad (1)$$

Through either Time Division Multiplexing (TDM) or Wavelength Division Multiplexing (WDM), a distributed array of FBGs inscribed in a single length of fiber can be interrogated with a single unit providing numerous spatially varying data points. To date, the use of dense ultra-short FBG arrays allow for the greatest multiplexing capability with demonstrations of over 600 discrete sensors per meter of fiber [21].

Current Commercial off the Shelf (COTS) FBG interrogator technology offers typical wavelength resolutions of 1 pm or 5 pm. Based on the initial sizing for the supersonic wind tunnel experiments – a compliant cantilever panel of dimensions 135 mm x 45 mm (length x width), can be used in conjunction with Euler-Bernoulli beam theory to determine the deflection sensitivity of the interrogation system. The resulting analysis (shown in Fig. 1) indicates that a coarse interrogator resolution will allow for deflections on the order of 50 to 5 microns to be measured, whilst the finer interrogator resolution can provide deflections on the order of 10 to 2 microns. While the cantilever case is basic, the principle applies to more complex geometries such as a clamped-free-clamped-free panel, where higher order modes will result in nodes and antinodes at different locations requiring an array of strain sensors [6].

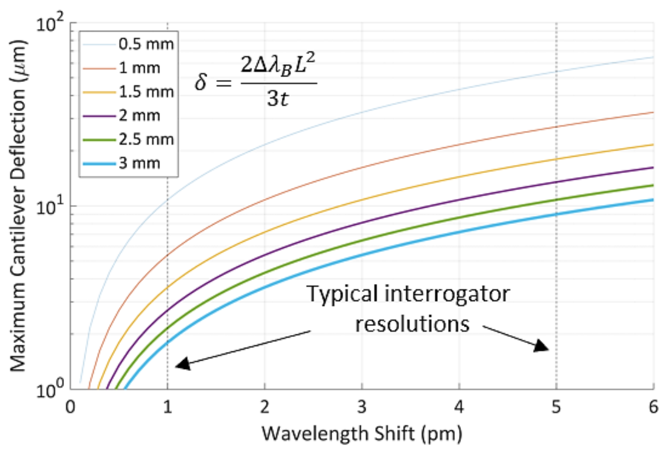

Figure 1. Sensitivity of an FBG to a vertical tip displacement of the cantilever beam used in the proceeding analyses.

II. Methodology and Results

A. Experimental Setup

The experimental campaign will be conducted in the supersonic blowdown wind tunnel at UNSW Canberra. The facility has several nozzles that can produce flow speeds between Mach 2 and Mach 3. A rigid steel forebody, dubbed the *hammerhead*, is mounted in the tunnel side walls. A cantilever panel is bonded to a steel insert which is then mechanically fastened to the hammerhead. This enables swapping of different panels with varying thickness and hence, levels of compliance. The model is also machined with internal channels for routing instrumentation including the OFS, strain gauges, and thermocouples. The leading edge of the hammerhead is constructed as a separate steel piece which is rigidly constrained on the hammerhead using a sliding T-slot. This also allows for the ability to change the leading-edge angle, as well as to lengthen and shorten the model. The assembled model and its location in the wind tunnel are shown in Fig. 2 below.

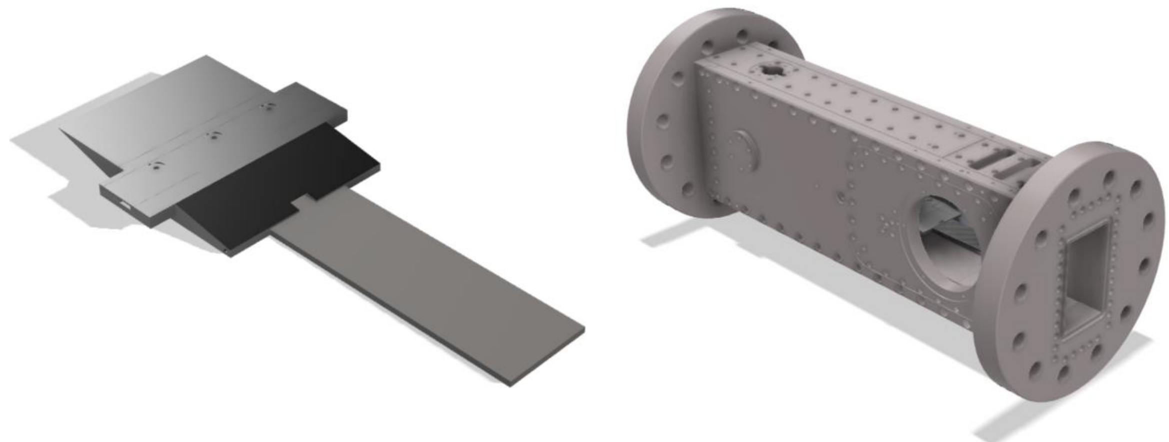

Figure 2. The cantilever model (left) and its mounted location in the tunnel (right).

The nature of the blowdown tunnel does not permit large models to be installed or the flow may begin to block. A typical rule of thumb employed for this facility is to ensure any model's projected frontal area is less than 10% of that of the tunnel cross-section. As such, with a nominal tunnel cross-section of 155 mm x 90 mm, any model must have a projected frontal area below 1,395 mm^2. This severely limits the ability to incline the cantilever model before the flow blocks. A relationship between model inclination angle and blockage percentage is given in Fig. 3 below. As evident, the maximum angle that could be employed to remain below the threshold is approximately 1.7° angle of attack. Such a shallow angle is unlikely to produce the dynamic response required for an FSI experiment. An alternative approach has hence been adopted wherein the leading-edge shock from the model is reflected off the tunnel walls to impinge upon the cantilever and therein produce an aerodynamic load that is sufficient to excite the model. This further allows for the study of FSI in the presence of a shock impingement.

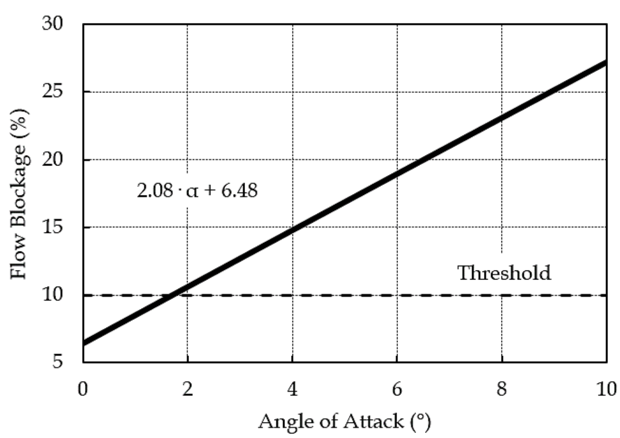

Figure 3. Tunnel flow blockage as a function of the model angle of attack

Moreover, because the mounting points in the tunnel walls are not located on the midplane, the model can be reflected asymmetrically to change the location of the shock impingement upon the cantilever. In this case, a "panel up" model results in a longer path length and has hence been used for the Mach 2 flow case. A "panel down" model has a shorter path length which aids in ensuring Mach 3 shock reflections can impinge. A diagram of the Mach 2 and 3 flow cases is shown below in Fig. 4.

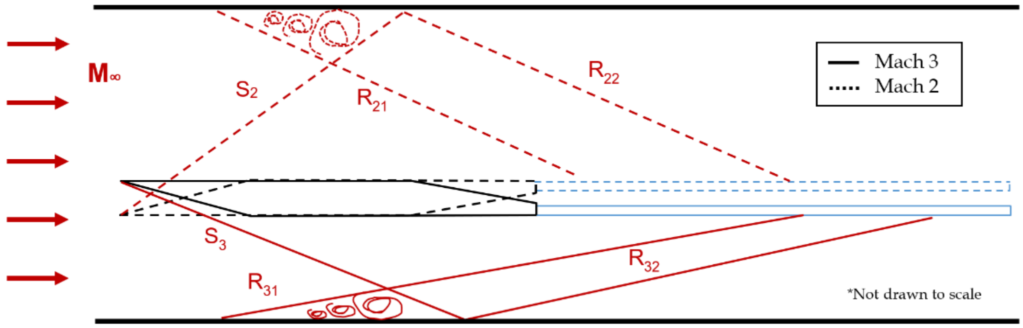

Figure 4. A representative schematic of the Mach 2 and Mach 3 flow cases.

The nominal freestream flow properties for both the Mach 2 and Mach 3 cases are given below. Dried air is supplied from a series of pressure reservoirs at ambient temperature. A pressure control valve is used to maintain a constant gauge pressure during the run. The control valve is used to feed a stagnation chamber before entering the test section.

Table 1. Nominal freestream flow properties for Mach 2 and Mach 3.

	Mach 2	Mach 3
Static Pressure (kPa)	25.56	9.528
Static Temperature (K)	166.7	107.1
Velocity (m/s)	517.6	622.3
Unit Reynolds Number (m^{-1})	8.103×10^{6}	10.72×10^{6}

To understand the current FSI case and how it compares to previous experimental work, a map of reduced frequency (f_r) versus aerodynamic to structural compliance ratio (Λ) has been employed. This map is recreated from [22] with the addition of the current work. As Λ increases, so too does the aerodynamic loads from the flow, shifting away from a structurally dominated response towards an aerodynamically dominated one. Similarly, a higher reduced frequency is indicative of a less compliant panel. The map given in Fig. 5 is demarcated into two distinct regions. Experiments on the right of the graph are typical of fully clamped experiments whilst those on the left are either cantilever or partially clamped. The planned experiments aim to fill a gap in the literature at lower reduced frequencies. Equations for f_r and Λ are given below where L is the total length of the plate, W is the width, f_s is the fundamental frequency in Hz, u_∞ is the freestream flow velocity, ρ_∞ is the freestream density, E is the Young's Modulus, I is the moment of inertia and M_∞ is the freestream Mach number.

$$f_r = \frac{L f_s}{u_\infty} \tag{2}$$

$$\Lambda = \frac{\rho_\infty u_\infty^2 W L^3}{E I M_\infty} \tag{3}$$

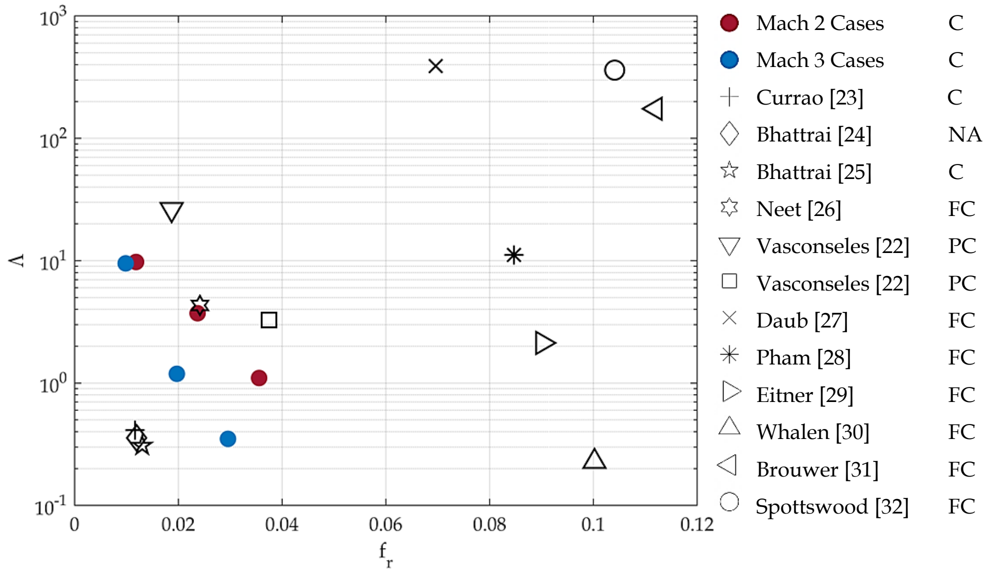

Figure 5. A map of reduced frequency and aerodynamic to structural compliance ratio for previous experimental work in FSI. C = Cantilever, FC = Fully Clamped, PC = Partially Clamped, NA = Not Available.

B. Numerical Methodology and Results

To estimate the deflections and strains experienced in the wind tunnel, a two-dimensional steady-state Computational Fluid Dynamics (CFD) solution is implemented. Static pressure traces along the top and bottom of the compliant panel are extracted, and their difference used as the input pressure for a transient Euler-Bernoulli beam solver. In this way, a rough estimation of the behavior of the compliant panel under the excitation load can be deduced without the computational overhead of a tightly coupled two-way FSI solution. In this approach, the deflections of the panel are not fed back to the CFD solver and hence, no aerodynamic stiffness or damping is incorporated. This can lead to severe overestimations of the panel deflection but is useful in early experimental design. Here, the one-way approach is simply used to generate strain signals as proof-of-concept for simulating the FBG signals. The fidelity of the data is not of the upmost importance as the methodology can be applied to any time-dependent strain signal.

In this case, the steady-state CFD solution of the flow is computed from the first throat up to the start of the converging section of the second throat. Simulations were obtained assuming fully laminar and fully turbulent flow, using Menter's Shear Stress Transport (SST) k-ω model. The SST k-ω model has been used due to its ease and general applicability.

Figure 6 shows a comparison between the laminar and turbulent solutions. It is quite clear from the comparison that a laminar assumption estimates a very large separation region resulting from shock impingement. The turbulent results produce a smaller separation region and stronger double shock reflection.

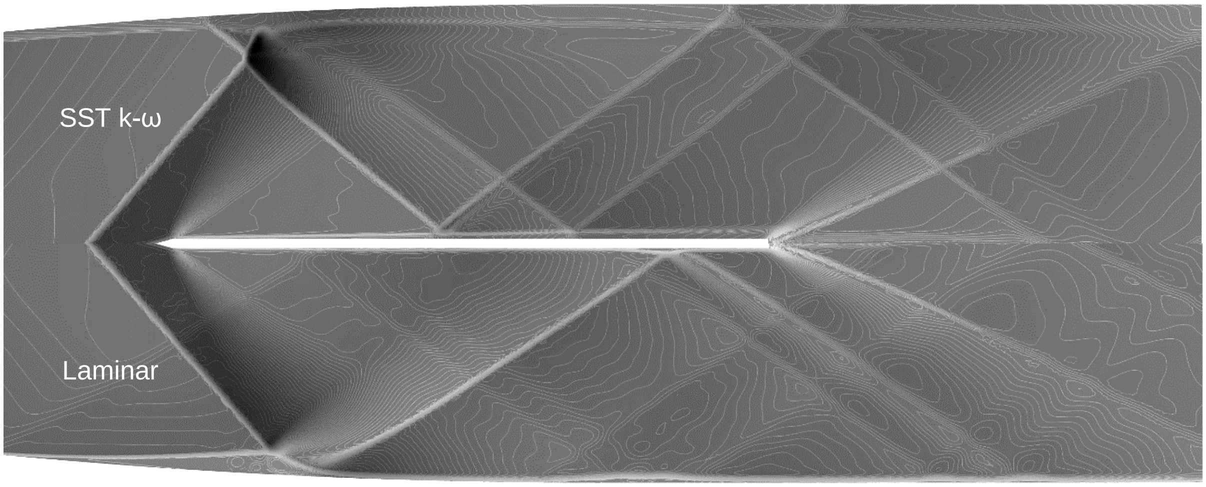

Figure 6. A comparison between Mach 2 solutions for SST k-ω (top) and laminar (bottom).

Early results from experimental testing indicate good agreement with steady-state CFD solutions. Figure 7 below is a comparison between images obtained from schlieren and density contours from the numerical solution. The numerical solution has been reflected about the midplane of the plate. The Reynold's Averaged Navier-Stokes (RANS) solution is not fully capturing all the detail in experiment; however, this is largely to be expected. The schlieren showcases several shocks that are not present in the numerical result, largely due to discontinuities and surface irregularities in the experimental model that have not been modelled numerically.

The comparison in Fig. 7 provides good agreement with the SST k-ω model and hence it can be reasonably assumed the flow is fully turbulent. This is furthermore a reasonable assumption to be made, considering the violent startup process that likely trips the flow quite early in the experimental run.

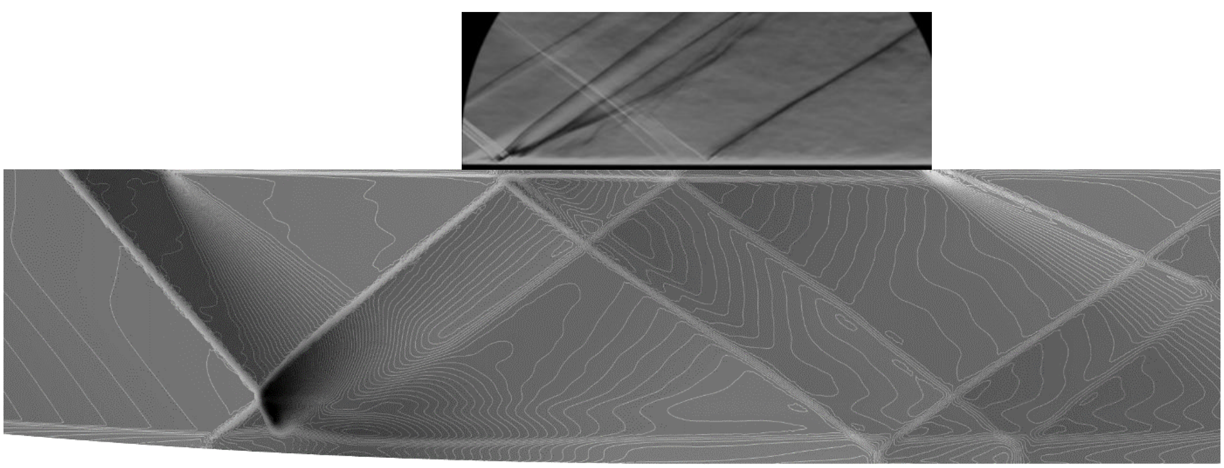

Figure 7. A comparison between numerical density contours and experimental schlieren. Numerical results are flipped vertically.

Pressure plots along the top and bottom sides of the plate for both Mach cases are shown in Fig. 8. As expected, the pressure difference is significantly higher for the Mach 2 case, producing a net negative pressure that would deflect the panel downwards. The Mach 3 case produces a higher pressure on the bottom of the plate, resulting in a net positive pressure that would deflect the panel upwards. Whilst the pressure loads in the Mach 2 case are significantly higher, the pressure loads at Mach 3 occur further along the panel, producing a larger bending moment.

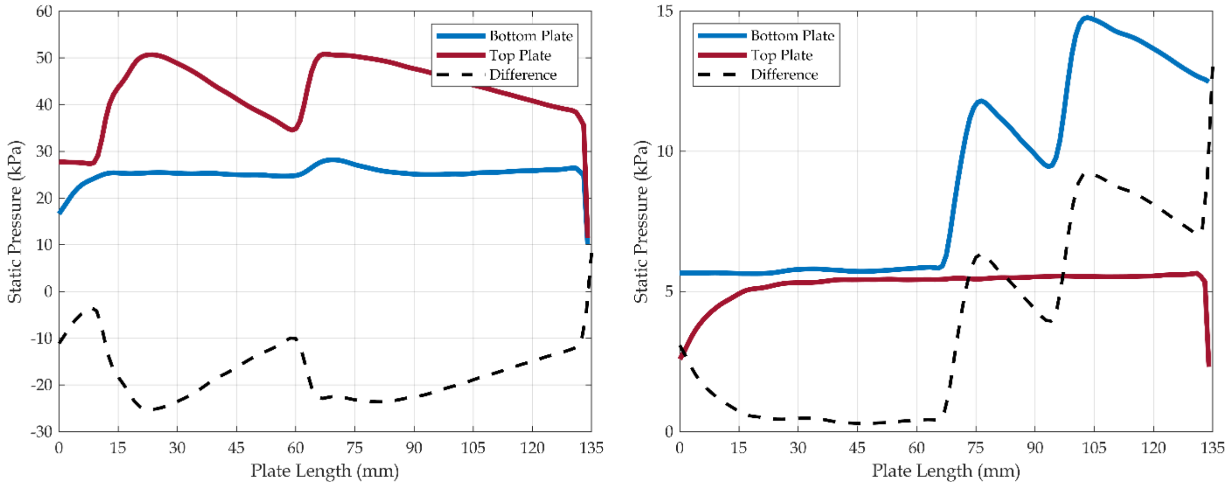

Figure 8. Pressure differences on the plate for the Mach 2 case (left) and Mach 3 (right).

C. Simulated FBG Response

To simulate the dynamic response of the panel, two FBG interrogation techniques are proposed. These are linear edge filter detection and power detection. The configurations of both are illustrated in Fig. 9.

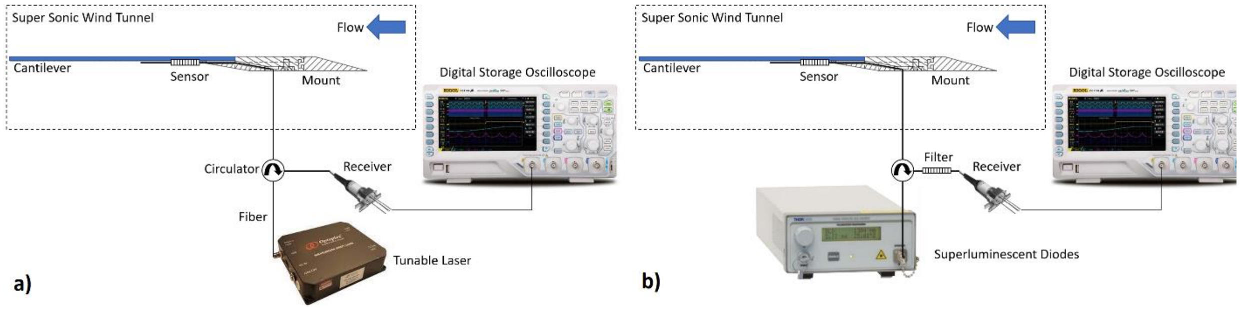

Figure 9. Experimental configuration for the a) laser-based power detection, and b) broadband light source-based edge filter detection.

For the power detection method, a tunable laser emits a specific wavelength in the bandwidth of the FBG. As the Bragg wavelength dynamically shifts, the magnitude of the received signal similarly changes. In this way, the FBG acts to modulate the reflected power of the tunable laser. Channel switching of the tunable laser allows it to constantly stay within a region of the reflected spectrum, even under high strains and temperatures. In the simulated results, a constant channel is maintained.

For the linear edge filter approach, the entire reflected spectrum is illuminated. A second, matched FBG which functions as a filter, has the same Bragg wavelength as the sensing FBG and blocks the entire returned spectra. As the sensing FBG is strained and the reflected spectra shifts, more power is transmitted. The operating principles of both methods are shown in Fig. 10 below.

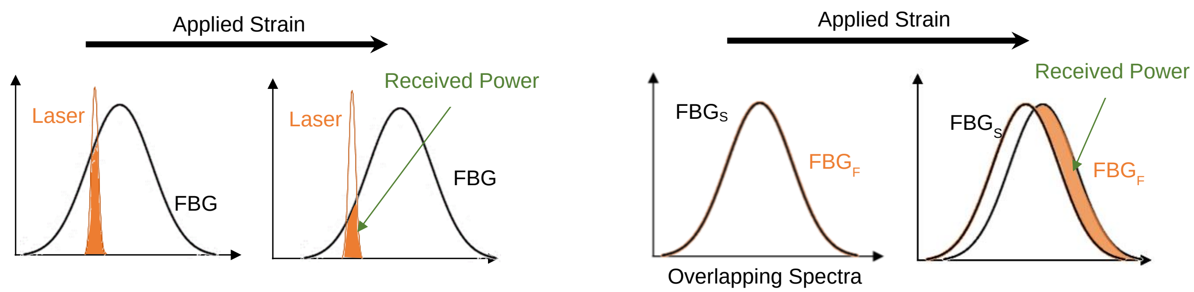

Figure 10. Operating principles of the power (left) and linear edge filter (right) detection methods.

Using both detection methods, an FBG is simulated halfway along the length of the cantilever panel as previously described. Results are obtained for panels of 3 mm, 2 mm, and 1 mm thicknesses. The 1 mm signal, as seen in Fig. 11, show saturation due to a shift in wavelength greater than the channel of the laser. It is evident that the power detection method produces signals of significantly higher gain compared to linear edge filter. Moreover, the linear edge filter appears to result in more noise, which is confirmed through calculation of the signal-to-noise ratios (SNR).

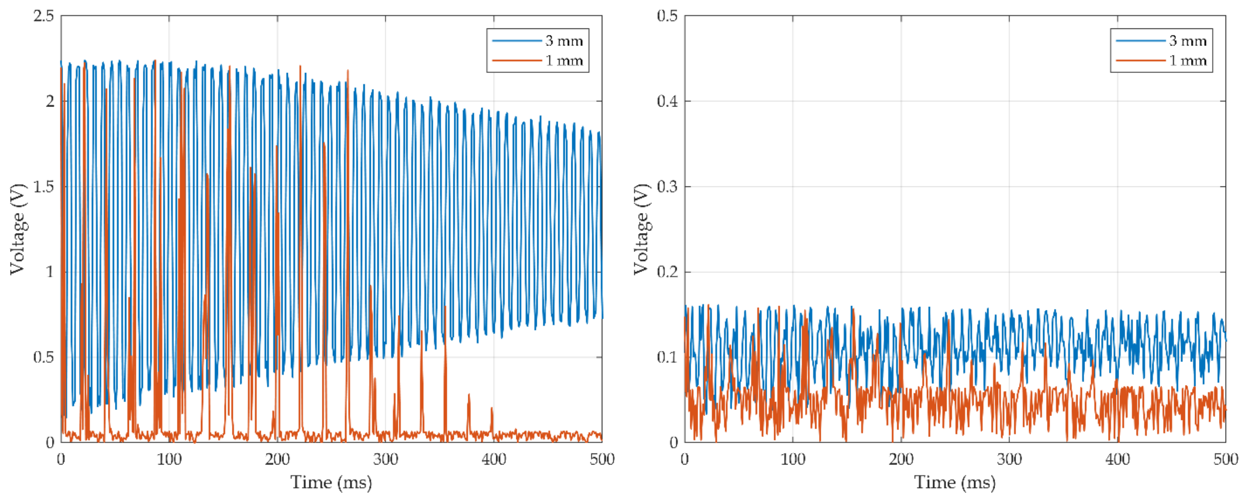

Figure 11. Time-domain signals acquired using the power detection (left) and linear edge filter (right) methods for the 3 mm and 1 mm plates.

Frequency obtained from the time-domain signals for both methods is shown in Fig. 12 at Mach 3. It is clear that the saturated 1 mm signal has resulted in the production of more spectral noise, including a large number of fingers at the different harmonics of the fundamental frequency. Despite this, the first mode frequency is still well predicted. The 3 mm plate shows the cleanest signal, appearing highly Gaussian, whereas the 2 mm plate shows some degree of saturation, it is still well characterized.

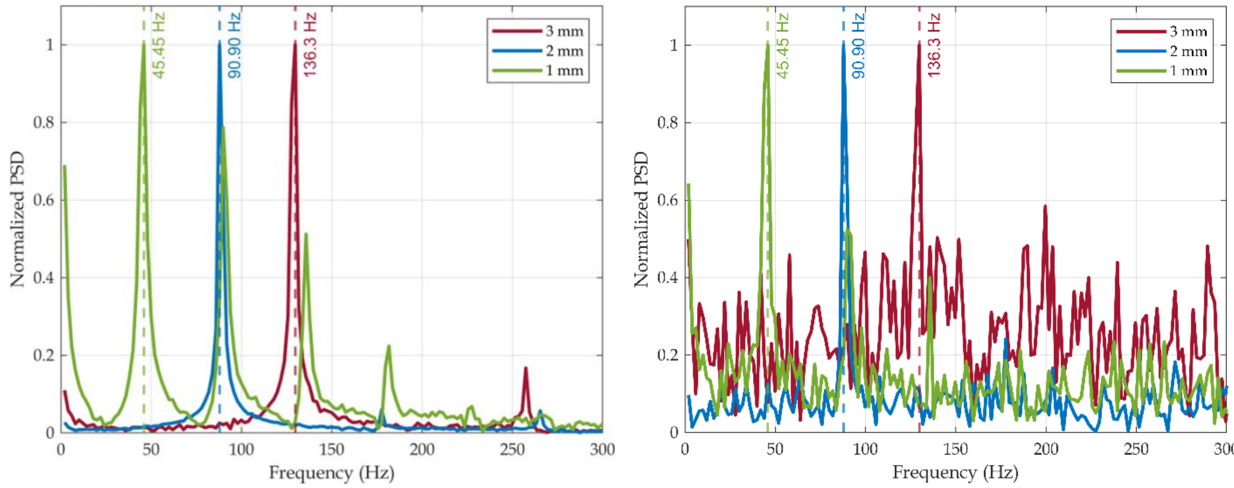

Figure 12. Frequency spectra of the acquired voltages using the power detection (left) and linear edge filter (right). Dotted vertical lines are the true peak frequencies of the respective thicknesses.

A final comparison is given in Fig. 13 for both methods with regard to the estimated SNR. When calculating the SNR, the first six harmonics of the signal are not considered noise. Both methods appear to be capable of predicting the peak frequency of each plate; however, as seen in Fig. 12, the 1 mm plate contains significant levels of spectral noise due to signal saturation, which is also confirmed in Fig. 13. For the power detection method, channel switching would be required to circumvent this. For the linear edge filter approach a long-period FBG (LP-FBG) can be used to significantly widen the filter and increase the dynamic range. LP-FBGs can easily have full-width half maximum values of over 5 nm [33].

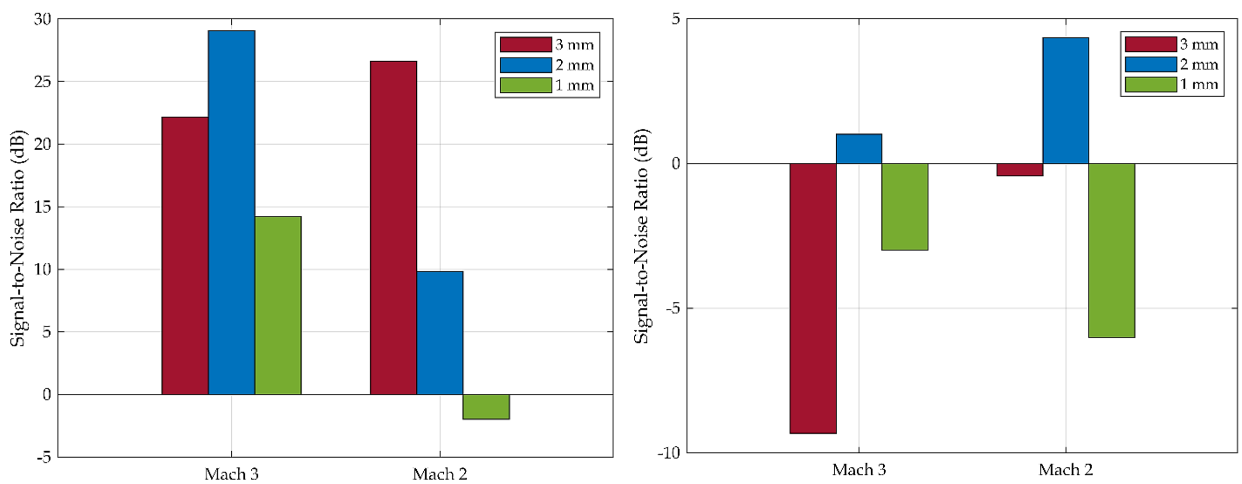

Figure 13. A comparison of the peak frequencies obtained from both methods.

III. Conclusion

This work has explored two different methods for simulating the response of a fiber Bragg grating sensor to a supersonic fluid-structurally induced oscillation on a cantilever plate. The FSI response of the cantilever is determined by solving a two-dimensional steady-state CFD solution and using the pressure difference on the plate to simulate the response of a Euler-Bernoulli beam. The one-way coupling approach adopted is not representative of the true FSI behavior of the plate, due to the lack of aerodynamic stiffness and damping. However, the ascertained strains are representative of FSI. In simulating the FBG signals a power based and linear edge filter method have been explored. Results indicate that the power detection method produces stronger signals with less noise but can be limited with regards to bandwidth. The ability to dynamically switch laser channels using a tunable laser would overcome this issue. Both methods are temperature insensitive and only capture the higher frequency dynamic signal, making them useful in temperature sensitive applications. Future work will explore applying these methods to a proposed experimental campaign.

Acknowledgments

This research was supported by the Air Force Office of Scientific Research under award number FA2386-22-1-4081. Any opinion, finding, and conclusions or recommendations expressed in this material are those of the authors and do not necessarily reflect the views of the United States Air Force. Numerical resources were provided by the National Computational Infrastructure (NCI), under the UNSW HPC Resource Allocation Scheme and the National Computational Merit Allocation Scheme (NCMAS) under project code fd8.

References

[1] L. Pollock, G. Wild, A. K. Abdelwahab, and J. Murray, "The Need for Aerospace Structural Health Monitoring: A review of aircraft fatigue accidents," *International Journal of Prognostics and Health Management,* vol. 12, no. 3, 2021, doi: https://doi.org/10.36001/ijphm.2021.v12i3.2368.

[2] L. Pollock and G. Wild, "An initial review of hypersonic vehicle accidents," presented at the 19th Australian International Aerospace Congress, Melbourne, Australia, 29 Nov. - 2 Dec., 2021, Conference Paper. [Online]. Available: https://arxiv.org/abs/2110.06438.

[3] Y. Guo *et al.*, "Investigation on aerothermodynamic environment and ablation which lead to HTV-2 second fight test failing," *Acta Aerodynamica Sinica,* vol. 35, no. 4, p. 496, 2017-08-25 2017, doi: https://doi.org/10.7638/kqdlxxb-2016.0114.

[4] T. G. Eason and S. Spottswood, "A Structures Perspective on the Challenges Associated with Analyzing a Reusable Hypersonic Platform," presented at the 54th AIAA/ASME/ASCE/AHS/ASC Structures, Structural Dynamics, and Materials Conference, Boston, MA, 8-11 Apr., 2013, Conference Paper. [Online]. Available: https://arc.aiaa.org/doi/abs/10.2514/6.2013-1747.

[5] L. Pollock and G. Wild, "Spectral Domain Analysis of Acousto-Ultrasonic Tone Burst Lamb Wave Emissions in Uncured Pre-Preg Carbon Fiber Composites," presented at the AIAA ASCEND, Las Vegas, NV, 15-17 Nov., 2021, Conference Paper. [Online]. Available: https://arc.aiaa.org/doi/abs/10.2514/6.2021-4233.

[6] L. Pollock and G. Wild, "Modal Analysis of a Scramjet Inlet for Optimization of Sensor Placement," presented at the AIAA ASCEND, Las Vegas, NV, 15-17 Nov., 2021, Conference Paper. [Online]. Available: https://arc.aiaa.org/doi/abs/10.2514/6.2021-4084.

[7] F. S. Kirkham and J. L. Hunt, "Hypersonic transport technology," *Acta Astronautica,* vol. 4, no. 1, pp. 181-199, 1977/01/01/ 1977, doi: https://doi.org/10.1016/0094-5765(77)90040-6.

[8] K. R. Brouwer and J. J. McNamara, "Enriched Piston Theory for Expedient Aeroelastic Loads Prediction in the Presence of Shock Impingements," *AIAA Journal,* vol. 57, no. 3, pp. 1288-1302, 2019, doi: https://doi.org/10.2514/1.J057595.

[9] G. M. D. Currao, A. J. Neely, C. M. Kennell, S. L. Gai, and D. R. Buttsworth, "Hypersonic Fluid–Structure Interaction on a Cantilevered Plate with Shock Impingement," *AIAA Journal,* vol. 57, no. 11, pp. 4819-4834, 2019, doi: https://doi.org/10.2514/1.J058375.

[10] S. Bhattrai, L. P. McQuellin, G. M. D. Currao, A. J. Neely, and D. R. Buttsworth, "Experimental Study of Aeroelastic Response and Performance of a Hypersonic Intake Ramp," *Journal of Propulsion and Power,* vol. 38, no. 1, pp. 157-170, 2022, doi: https://doi.org/10.2514/1.B38348.

[11] P. B. Vasconcelos, L. McQuellin, K. Talluru, and A. Neely, "Hypersonic Fluid-Structure Interactions on a Compliant Clamped-Free-Clamped-Free Panel Under the Influence of Static Shock Impingement," presented at the AIAA SCITECH 2022 Forum, San Diego, CA, 3-7 Jan., 2022, Conference Paper. [Online]. Available: https://arc.aiaa.org/doi/abs/10.2514/6.2022-0241.

[12] X. Gui *et al.*, "High-Density Distributed Crack Tip Sensing System Using Dense Ultra-Short FBG Sensors," *Sensors,* vol. 19, no. 7, p. 1702, 2019. [Online]. Available: https://www.mdpi.com/1424-8220/19/7/1702.

[13] L. P. McQuellin, A. Neely, and G. Currao, "Considerations for a Hypersonic Flight Test Investigating Fluid-Thermal-Structural Interactions," presented at the 23rd AIAA International Space Planes and Hypersonic Systems and Technologies Conference, Montreal, Canada, 10-12 Mar., 2020, Conference Paper. [Online]. Available: https://arc.aiaa.org/doi/abs/10.2514/6.2020-2419.

[14] A. A. Phoenix, J. R. Maxwell, and G. B. Goodwin, "Morphing High-Temperature Surfaces for Shapeable Hypersonic Waverider Vehicles," presented at the ASME 2017 Conference on Smart Materials, Adaptive Structures and Intelligent Systems, Snowbird, UT, 18-20 Sep., 2017, Conference Paper. [Online]. Available: https://doi.org/10.1115/SMASIS2017-3766.

[15] G. Wild and S. Hinckley, "Acousto-Ultrasonic Optical Fiber Sensors: Overview and State-of-the-Art," *IEEE Sensors Journal,* vol. 8, no. 7, pp. 1184-1193, 2008, doi: https://doi.org/10.1109/JSEN.2008.926894.

[16] G. Wild, "Novel photonics sensing and systems for military metrology," in *2015 IEEE Metrology for Aerospace (MetroAeroSpace),* 2015: IEEE, pp. 129-134, doi: https://doi.org/10.1109/MetroAeroSpace.2015.7180640.

[17] P. Calhoun, "DARPA Emerging Technologies," *Strategic Studies Quarterly,* vol. 10, no. 3, pp. 91-113, 2016. [Online]. Available: http://www.jstor.org/stable/26271496.

[18] G. Wild, "Optical fiber bragg grating sensors applied to gas turbine engine instrumentation and monitoring," presented at the IEEE Sensors Applications Symposium (SAS), Galveston, TX, 19-21 Feb., 2013, Conference Paper. [Online]. Available: https://ieeexplore.ieee.org/abstract/document/6493583.

[19] C. R. Liao and D. N. Wang, "Review of femtosecond laser fabricated fiber Bragg gratings for high temperature sensing," *Photonic Sensors,* vol. 3, no. 2, pp. 97-101, 2013/06/01 2013, doi: https://doi.org/10.1007/s13320-012-0060-9.

[20] A. Othonos and K. Kalli, *Fiber Bragg Gratings: Fundamentals and Applications in Telecommunications and Sensing*. Artech House, 1999.

[21] G. Xin *et al.*, "Distributed sensing technology of high-spatial resolution based on dense ultra-short FBG array with large multiplexing capacity," *Opt. Express,* vol. 25, no. 23, pp. 28112-28122, 2017/11/13 2017, doi: https://doi.org/10.1364/OE.25.028112.

[22] P. B. Vasconcelos, L. P. McQuellin, T. Krishna, and A. Neely, "Experimental Study of Hypersonic Fluid-Structure Interactions on an Inclined Clamped-Free-Clamped-Free Compliant Panel," in *ASCEND 2021*, 2021, p. 4232.

[23] G. M. Currao, A. J. Neely, D. R. Buttsworth, and S. L. Gai, "Hypersonic fluid-structure interaction on a cantilevered plate," in *7th European Conference for Aeronautics and Space Sciences*, 2017, vol. 12, p. 13, doi: https://doi.org/10.2514/1.J058375.

[24] S. Bhattrai, L. P. McQuellin, G. Currao, A. Neely, and D. R. Buttsworth, "Experimental study of the aeroelastic response and performance of a hypersonic intake," in *23rd AIAA International Space Planes and Hypersonic Systems and Technologies Conference*, 2020, doi: https://doi.org/10.2514/6.2020-2449.

[25] S. Bhattrai, L. McQuellin, G. M. Currao, A. Neely, and D. Buttsworth, "Influence of hypersonic fluid-structure interaction on the control authority of a trailing-edge flap," in *22nd AIAA International Space Planes and Hypersonics Systems and Technologies Conference*, 2018, p. 5265, doi: https://doi.org/10.2514/6.2018-5265.

[26] M. C. Neet and J. M. Austin, "Effects of surface compliance on shock boundary layer interaction in the caltech mach 4 ludwieg tube," in *AIAA Scitech 2020 forum*, 2020, p. 0816, doi: https://doi.org/10.2514/6.2020-0816.

[27] D. Daub, B. Esser, and A. Gülhan, "Experiments on high-temperature hypersonic fluid–structure interaction with plastic deformation," *AIAA Journal,* vol. 58, no. 4, pp. 1423-1431, 2020, doi: https://doi.org/10.2514/1.J059150.

[28] H. T. Pham, Z. N. Gianikos, and V. Narayanaswamy, "Compression ramp induced shock-wave/turbulent boundary-layer interactions on a compliant material," *AIAA Journal,* vol. 56, no. 7, pp. 2925-2929, 2018, doi: https://doi.org/10.2514/1.J056652.

[29] M. A. Eitner, Y.-J. Ahn, L. Vanstone, M. N. Musta, J. Sirohi, and N. Clemens, "Effect of shock-wave boundary layer interaction on vibratory response of compliant panel," in *AIAA Aviation 2021 Forum*, 2021, p. 2493, doi: https://doi.org/10.2514/6.2021-2493.

[30] T. J. Whalen *et al.*, "Hypersonic fluid–structure interactions in compression corner shock-wave/boundary-layer interaction," *AIAA journal,* 2020, doi: https://doi.org/10.2514/1.J059152.

[31] K. R. Brouwer, R. Perez, T. J. Beberniss, S. M. Spottswood, and D. A. Ehrhardt, "Fluid-structure interaction on a thin panel including shock impingement effects," in *AIAA Scitech 2021 Forum*, 2021, p. 0910, doi: https://doi.org/10.2514/6.2021-0910.

[32] S. M. Spottswood *et al.*, "Exploring the response of a thin, flexible panel to shock-turbulent boundary-layer interactions," *Journal of Sound and Vibration,* vol. 443, pp. 74-89, 2019, doi: https://doi.org/10.1016/j.jsv.2018.11.035.

[33] Y. Bian, K. Jiao, X. Wu, H. Shen, F. Yang, and R. Zhu, "Utilizing phase-shifted long-period fiber grating to suppress spectral broadening of a high-power fiber MOPA laser system," *High Power Laser Science and Engineering,* vol. 9, p. e39, 2021, doi: https://doi.org/10.1017/hpl.2021.26.